Designing the perovskite structural landscape for efficient blue emission

Natalia Yantara [a,+], Nur Fadilah Jamaludin [b,+], Benny Febriansyah [a], David Giovanni [c], Annalisa Bruno [a], Cesare Soci [c], Tze Chien Sum [c], Subodh Mhaisalkar [b,], and Nripan Mathews [b,*]*

[a] Energy Research Institute @ NTU, Nanyang Technological University, Research Techno Plaza, X-Frontier Block, Level 5, 50 Nanyang Drive, 637553, Singapore

[b] School of Materials Science and Engineering, Nanyang Technological University, 50 Nanyang Avenue, 639798, Singapore

[c] Division of Physics and Applied Physics, School of Physical and Mathematical Sciences, Nanyang Technological University, 21 Nanyang Link, 637371, Singapore

[+] The authors contribute equally in this article.

Corresponding Authors

* Subodh Mhaisalkar (Email: Subodh@ntu.edu.sg)

* Nripan Mathews (Email: Nripan@ntu.edu.sg)

Abstract

Despite rapid development of perovskite light emitting diodes (PeLEDs) in recent years, blue PeLEDs' efficiencies are still inferior to their red and green counterparts. The poor performance is associated with, amongst other factors, halide-segregation in bromide-chloride materials and energy funneling to lowest bandgaps in multi-layered Ruddlesden Popper (RP) systems. This study reports that compositional engineering through prudent selection of A-site cation in a pure bromide RP system, a narrow distribution of layered domains can be achieved. With a narrow distribution centred around the desired RP domain, efficient energy cascade to yield blue emission is ensured. Coupled with rapid nucleation induced by antisolvent deposition technique, record efficiencies of 2.34 and 5.08%, corresponding to colour-stable deep blue (~ 465 nm) and cyan (~ 493 nm) respectively, were attained. This composition and process engineering to design favorable structural landscape is transferrable to other material systems which paves the way for high performance PeLEDs.

TOC GRAPHICS

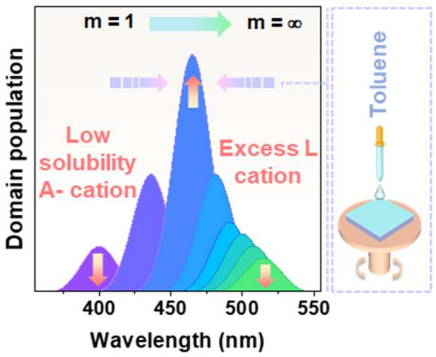

Halide compounds with ABX_3 perovskite structure (where A, B and X are monovalent cation, divalent cation and halide anion respectively) are attractive for optoelectronic research owing to their unique properties such as long carrier diffusion lengths[1–3], low trap densities[4], tunable bandgaps[5] and high luminescence quantum yields[6]. Within five years, rapid progress in perovskite-based light emitting devices (PeLEDs) research drove the efficiency increase from <1%[7] to 20%[8,9]. Nevertheless, the efficiency strides have been noted only for green and red emissions – with the efficiency for blue-emitting PeLEDs still wanting. Although wide bandgap perovskites are achievable by employing chloride, the penchant for deep trap states formation increases non-radiative recombination[10]. Attempts to yield blue emission through partial bromide substitution are afflicted with colour instability and low efficiency due to reduced photoluminescence quantum yield (PLQY) and electric field-induced halide segregation[11]. Therefore, it is imperative that an alternative strategy be devised to obtain spectrally stable blue PeLEDs (bandgap, $E_g \geq 2.48 – 2.56$ eV).

Another approach involves the substitution of A-site cation with spacer molecules (L) resulting in the formation of Ruddlesden-Popper (RP) perovskites with reduced $[BX_6]$ octahedral network connectivity[12]. On introducing monovalent ammonium molecules, layered RP perovskite with chemical formula $L_2A_{m-1}B_mX_{3m+1}$ is produced, depending on the degree of L cation incorporation into the crystal structure (m). While E_g can be widened by decreasing the number of m layers[13], incorporating more insulating L cations would impede carrier transport[14]. This underscores the need for emissive perovskite layers consisting of an intermediate number of m layers to satisfy both E_g and charge transport criteria. However, depositing phase pure $m \geq 2$ films is a challenge due to (1) the progressively smaller difference in thermodynamic stability of phases with increasing number of m layers, and/or (2) the propensity for $m = 1$ formation due to strong van der

Waals interactions between L–L cations which will deplete the concentration of L cation in the reservoir and thus encourage formation of heterogeneous films[15]. Formation of mixed-dimensional RP perovskite film promotes energy transfer to the smallest E_g domains which facilitates the fabrication of high efficiency PeLEDs[16,17]. Conversely, efficient energy cascade from high E_g domains (donor) to low E_g domains (acceptor) reveals the need to eliminate formation of $m \approx \infty$ domains to achieve colour-pure blue-emitting RP perovskite.

Previous reports have shown that excess L cation is needed to tailor the m domain distribution. For example, a complex 4-cation system can be employed to control the m domain distribution which results in PeLED with external quantum efficiency (EQE) of 1.5% at 490 nm electroluminescence (EL) peak emission[15]. A triple cation strategy where RP perovskite alloyed with Rb is coupled with in-situ passivation, has enabled PeLEDs with EQE of 1.35% at 475 nm peak emission[18] to be produced. Recently, another triple cation approach to form nanoparticles within RP phases yielding EQE of 9.5% at 483 nm peak emission was reported [19]. Despite the high efficiency, the lack of in-depth studies on the crystallization kinetics of RP perovskite highlights the need for a more systematic study on cation interactions.

Here, the crystallization kinetics of RP perovskite is assessed, allowing for the tailoring of narrow and intermediate m domains through compositional engineering of simple bi-cationic systems. We postulate that by introducing excess L cation together with a low solubility A-site cation to promote fast nucleation, a narrow, monodispersed distribution of intermediate m domains centered at the desired blue emission peak, can be attained. In conjunction, process engineering to induce fast nucleation further reduces the m domain distribution. Those strategies enable us to achieve efficient and spectrally stable PeLEDs spanning the entire blue region with EQEs of 2.34, 4.34, and 5.08% at EL peak wavelengths of 465, 486, and 493 nm respectively. The applicability

of this concept to other L cation systems, showcases the broader impact of this study towards the development of efficient PeLEDs.

To obtain intermediate m domains, m =1 domain formation is suppressed by employing low solubility bromide salt to boost the incorporation of A-site cation whereas excess L cation is used to curb formation of m = ∞ domains (**Figure 1a**). Toluene is introduced as an antisolvent during spin coating to promote fast nucleation rate, thus reducing the m domain distribution further. Three bromide salts of different A-site cation are compared, i.e. formamidinium bromide (FABr), methylammonium bromide (MABr), and cesium bromide (CsBr). Bulk solubility of these cations in a mixed DMF – DMSO co-solvent are found to be 10 M, 5 M, and 0.05 M respectively.

The capability of L cation: 4-phenyl-1-butylammonium cation ($C_6H_5(CH_2)_4NH_3^+$, referred to as PBA^+) to form m = 1 RP perovskite is confirmed by X-Ray diffraction (XRD) analysis (**Supplementary Note 1**) with excitonic absorbance and photoluminescence (PL) peak features noted at 393 and 405 nm, respectively (**Figure 1b**). Difficulties in obtaining pure $m \geq 2$ RP phases from both homogeneous[20] and heterogeneous[21,22] nucleation methods are known and therefore, for simplicity, <m> is used to represent the stoichiometric ratio in the precursor solution while m denotes the actual number of [$PbBr_6$] layers present in the system. A-site cation variation does not appear to affect the roughness (~ 2 nm) and thickness (~ 30 nm) of these films (**Figure S1**).

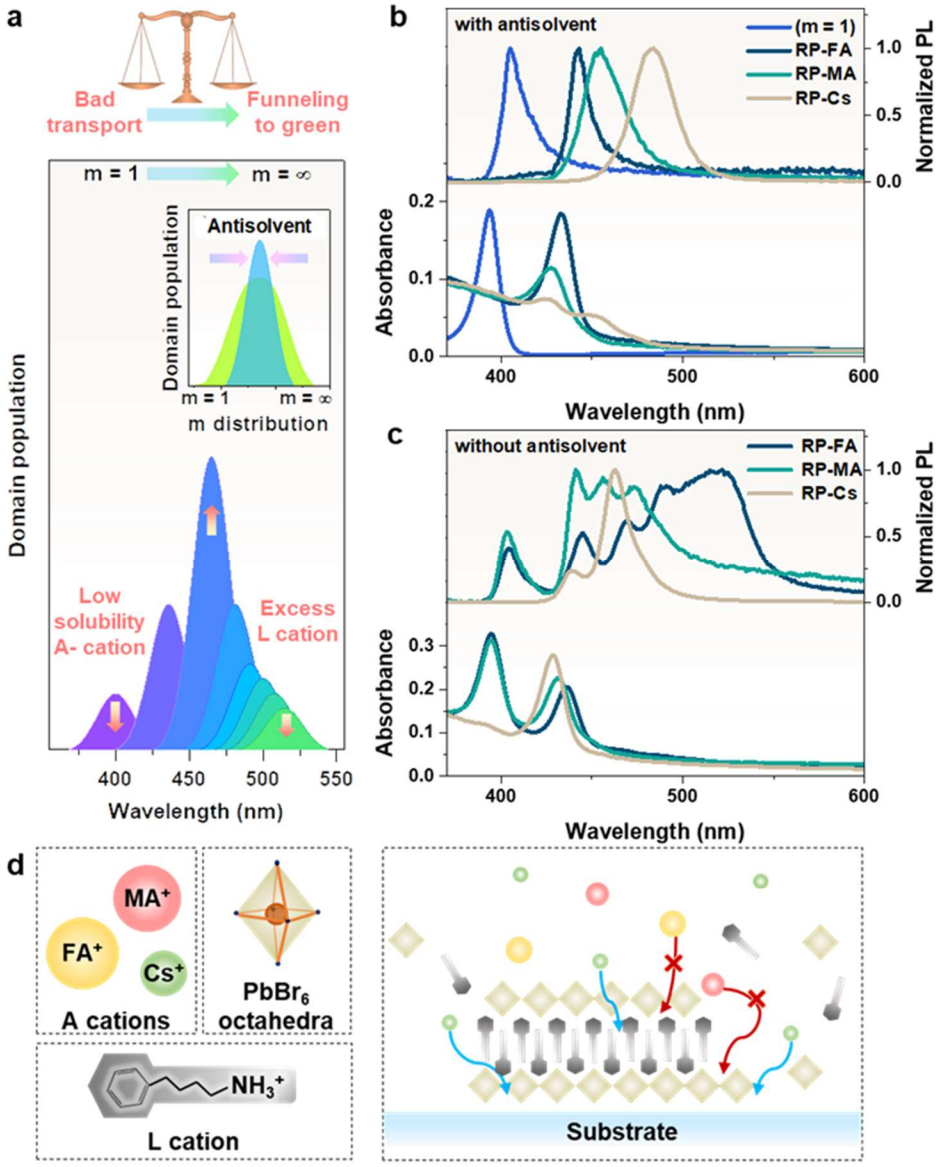

Figure 1. Strategy and mechanism to create pure blue emissive RP perovskite ($L_2A_{m-1}B_mX_{3m+1}$ with *m* corresponding to the degree of L cation incorporation). Schematic diagram representing the strategy adopted to form intermediate *m* domains for blue emissive RP films with PBA^+ as L cation, where increasing concentration of low-solubility A-cation and introducing excess L cation in the perovskite precursor solution suppresses the formation of $m = 1$ and $m = \infty$ domains (a). Inset of panel (a) illustrates the effect of antisolvent treatment on *m* domain distribution. The absorbance and normalized photoluminescence spectra of PBA_2PbBr_4 (m = 1) and RP films prepared from $\langle m \rangle = 2$ solutions with different A-site cations with (b) and without (c) antisolvent indicate that *m* domain distribution can be narrowed by employing both low solubility A-site cation and antisolvent treatment. The schematic diagram of proposed RP formation mechanism highlighting the formation of intermediate *m* domains by the favorable incorporation of small size and low-solubility A-site cation (Cs^+) into $m = 1$ system (d).

The low solubility A-site cation salt (Cs^+) is expected to limit formation of m =1 and promote intermediate m domain formation due to the higher tendency to reach supersaturation. For <m=2> system, employing high solubility FA^+ results in a wide distribution of m domains as reflected in the RP-FA PL spectra where multiple peaks (405 to 525 nm) corresponding to m = 1 and m values approaching ∞, are observed (**Figure 1c**). Multiple PL peaks (405 to 474 nm) with narrow peak distribution, tentatively assigned to m = 1 and m = 4, are produced when less soluble MA^+ cation is utilized. Further narrowing of PL peak distribution ranging from 438 to 463 nm is obtained when Cs^+, the cation with the lowest bulk solubility, is employed. These arise due to the favourable formation of m = 1 during the early nucleation stage which reduces the L cation reservoir and facilitates growth of higher m domains (including ∞). This effect is evident for the highly soluble FA^+, where its slow incorporation into the low m domain leads to the formation of higher m domains and a larger PL peak distribution. For low solubility Cs system, the situation is reversed and rapid incorporation of Cs yields RP-Cs films with intermediate domains. Hence, we propose that the formation of low m domains is kinetically favoured during the initial stages of RP film growth due to strong van der Waals interaction between the L cations[15,23]. As the film growth proceeds, the A-site cation gets incorporated into the PBA^+ bilayer and form higher m domains[24] (**Figure 1d**). The large size and high solubility of FA^+ cation promote phase separation in the system as it is not readily incorporated for growth of low m domains, unlike the Cs^+ cation, where its small size and low solubility allow for easy incorporation into the low m domains to form narrowly distributed intermediate m domains.

In addition to compositional engineering, variations to nucleation and growth kinetics during film preparation also modulate the distribution of m-domains in RP perovskites. Deposition

methods involving slow and fast supersaturation processes were investigated by employing the conventional and antisolvent assisted spincoating procedures. The antisolvent technique induces fast supersaturation state, leading to smaller PL FWHM and lesser absorbance excitonic peaks due to the narrower m distribution across all systems regardless of the choice of antisolvent, A-site, and L cations (**Figure 1b, S2, Supplementary Note 2 and 3**). This concurs with the LaMer burst model[24,25], where a high rate of nucleation within a short period of time followed by slow rate of growth over a longer period promote the formation of monodispersed colloids and vice versa. Hence, aside from employing the compositional engineering strategy, antisolvent is also crucial to achieve a narrow m domain distribution.

To verify RP perovskite formation mechanism, the absorbance spectra as a function of time on introduction of perovskite precursor solution into the antisolvent, are monitored (**Figure S3**). As heterogeneous nucleation readily occurs at lower saturation as compared to homogeneous system, perovskite precursor solution is added to the antisolvent to mimic fast heterogeneous nucleation. The appearance of excitonic absorbance peak confirms the formation of RP perovskite. For RP-FA and RP-MA systems, the formation of m = 2 particles, as indicated by excitonic absorbance features at 433 nm and 429 nm respectively, occur instantaneously on addition of <m> = 2 precursor solution. This can be explained by the stronger hydrogen bonding between the organic A-site cation (FA^+ and MA^+) and the inorganic octahedra[26]. Increasing the reaction time promotes particle growth as noted by the higher light scattering especially at longer wavelengths. On the other hand, as the reaction progresses, the absorbance shoulder at 450 nm becomes increasingly prominent, indicating higher amount of m > 2 nanoparticles forming in the RP-MA system after 40 s. In contrast, m = 1 particles with excitonic absorbance peak at 399 nm are the first to form for RP-Cs system despite Cs^+ (~0.05M) lower bulk solubility limit as compared to PBA^+ (~5M) in the

DMF – DMSO co-solvent. With increasing reaction time, formation of higher m nanoparticles becomes evident with signature of assigned m = 2 (at 429 nm) and m = 3 (at 456 nm) observed after 40 s. This observation is consistent with the hypothesis that the formation of low m nanoparticles is kinetically favoured prior to growth of higher m nanoparticles. The rate of growth for higher m nanoparticles is faster for Cs^+ due to the smaller cation size and lower solubility.

Transient absorption (TA) spectroscopy, PL excitation spectra, and time resolved photoluminescence (TRPL) data reveal the efficient energy cascade process from donor to acceptor domains in RP-Cs prepared with antisolvent processing (**Supplementary Note 4**), highlighting the need to completely eliminate $m \approx \infty$ domains for pure blue EL. Energy cascade process is also observed from TA spectra of RP-FA and RP-MA, with higher signal of high m domains detected for RP-FA, followed by RP-MA, and RP-Cs respectively (**Supplementary Note 4**). PeLEDs based on these systems, with standardized hole transporting material (HTL) and electron transporting material (ETL), are fabricated (**Figure 2a**). RP-Cs displays the lowest turn-on voltage (V_{th} ~2.9V) indicating balanced charge injection among the three systems (**Figure 2b**). The energy cascade phenomenon is modulated by varying the donor to acceptor ratio, where efficient energy funneling results in an EQE boost while high donor to acceptor ratio leads to inefficient energy cascade and results in peak asymmetry or multiple emission peaks with low EQE[27]. Lower EQE and multiple EL peaks (**Figure 2c-d and S4**) are observed for both RP-FA (~ 0.002%) and RP-MA (~0.03%) systems due to the higher donor to acceptor ratio, which is in agreement with the PL data. On increasing applied bias, the EL spectra blue shifts, signifying incomplete energy transfer to the lowest E_g domain arising from insufficient acceptor concentration[27]. RP-Cs systems yield spectrally stable devices as the narrower m distribution offers an ideal donor to acceptor ratio guaranteeing high efficiency (~1.29%)[27]. Poor spectral stability

for devices prepared with conventional spincoating process (**Figure S5**), further highlights the importance of the antisolvent technique for optimum donor to acceptor ratio. Hence, our study provides clear explanation for the domination of Cs^+ system in most reports for blue RP-based PeLEDs (**Table S1**).

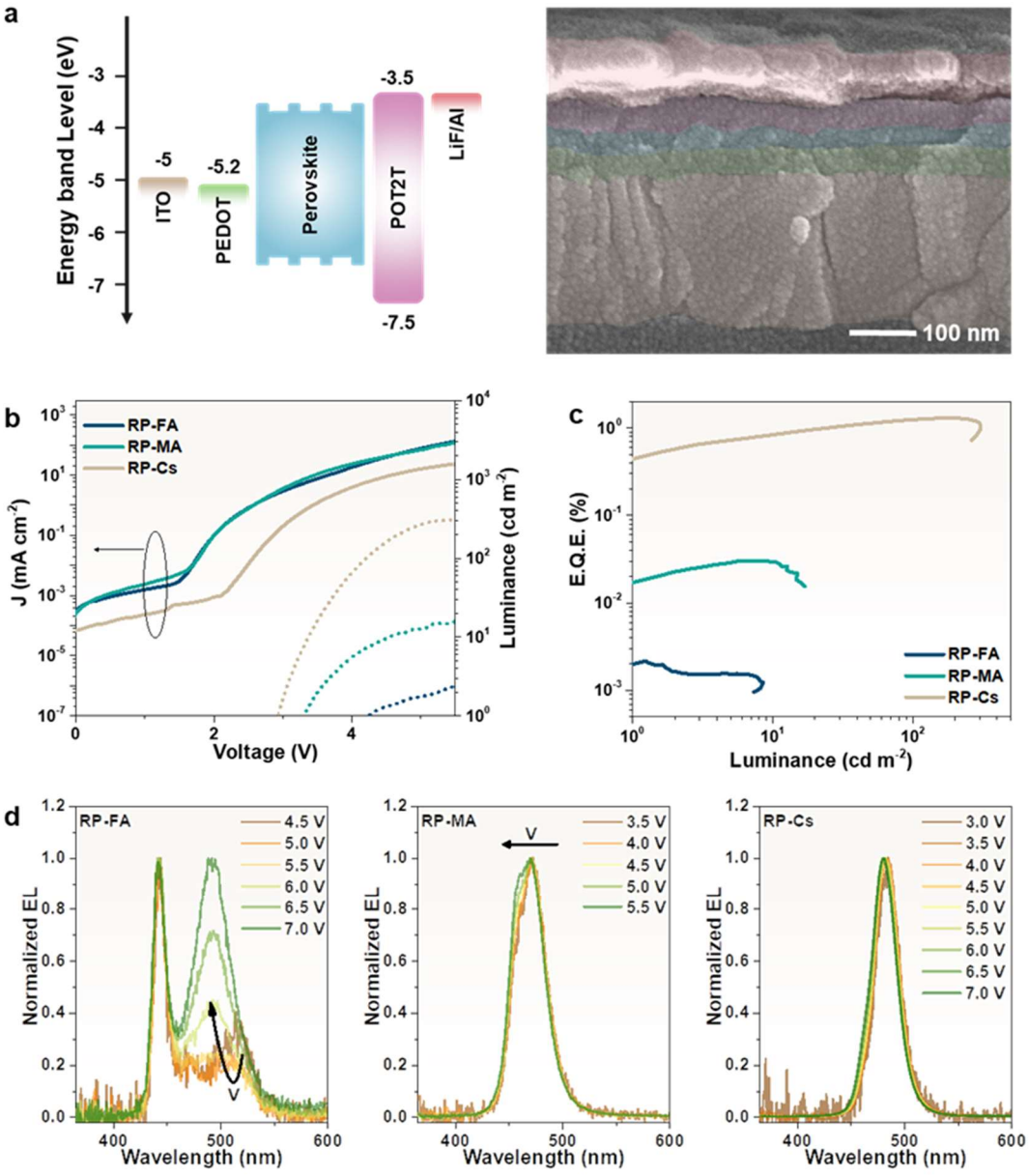

Figure 2. Electrical and optical characteristics of RP-based PeLEDs. Energy band alignment of the different layers in the device stack together with the corresponding cross-sectional image (a). The current density (J) and luminance response as a function of voltage (b), the EQE versus

luminance (c) for devices deposited from <m> = 2 precursor solutions of RP-FA, RP-MA, and RP-Cs. The corresponding normalized EL spectra at various applied bias (d) provide evidence that spectrally stable devices can be obtained from RP-Cs system by forming a narrow intermediate m domain distribution. The blue shifting of RP-FA and RP-MA EL spectra at high applied bias reveal the non-ideal high E_g (donor) to low E_g (acceptor) domain ratio.

To vary the emission colour, fine-tuning of PBA and Cs concentrations is pursued. Although <m> = 2 was used, majority of the emission comes from m = 4 – 5 with EL peak at 486 nm. In the regular <m> = 2 solution with excess PBA, PBA/Pb ratio is set at 1.5 whereas PBA/Cs ratio is fixed at 3.3. We deduce that both PBA/Pb and PBA/Cs ratios play significant roles in controlling the proportion of intermediate m domains. To attain deep blue emission (~460 nm), narrow spread of lower intermediate m domains (m = 3 – 4) is achieved by slightly increasing the PBA/Pb precursor ratio. Meanwhile, although lowering Cs content enables tuning of PL emission, sufficient Cs^+ supply is required to maintain high PL intensity as acceptor domain concentration grows with increasing Cs incorporation into low m domains. This prediction is in good agreement with the systematic blue shift of the PL peak and absorbance onset when PBA/Pb ratio is increased up to 1.7; due to the preferred formation of lower intermediate m domains (**Figure S6**). Increasing the PBA/Cs ratio to 5 results in less acceptor domains relative to the donor domains which translates to multiple PL peaks regardless of the PBA/Pb ratio. Lowering the PBA/Cs ratio on the other hand, slightly red shifts the PL and enhances the PL intensity of film regardless of PBA/Pb ratio due to the more efficient energy cascade with higher acceptor concentration (**Figure S6**).

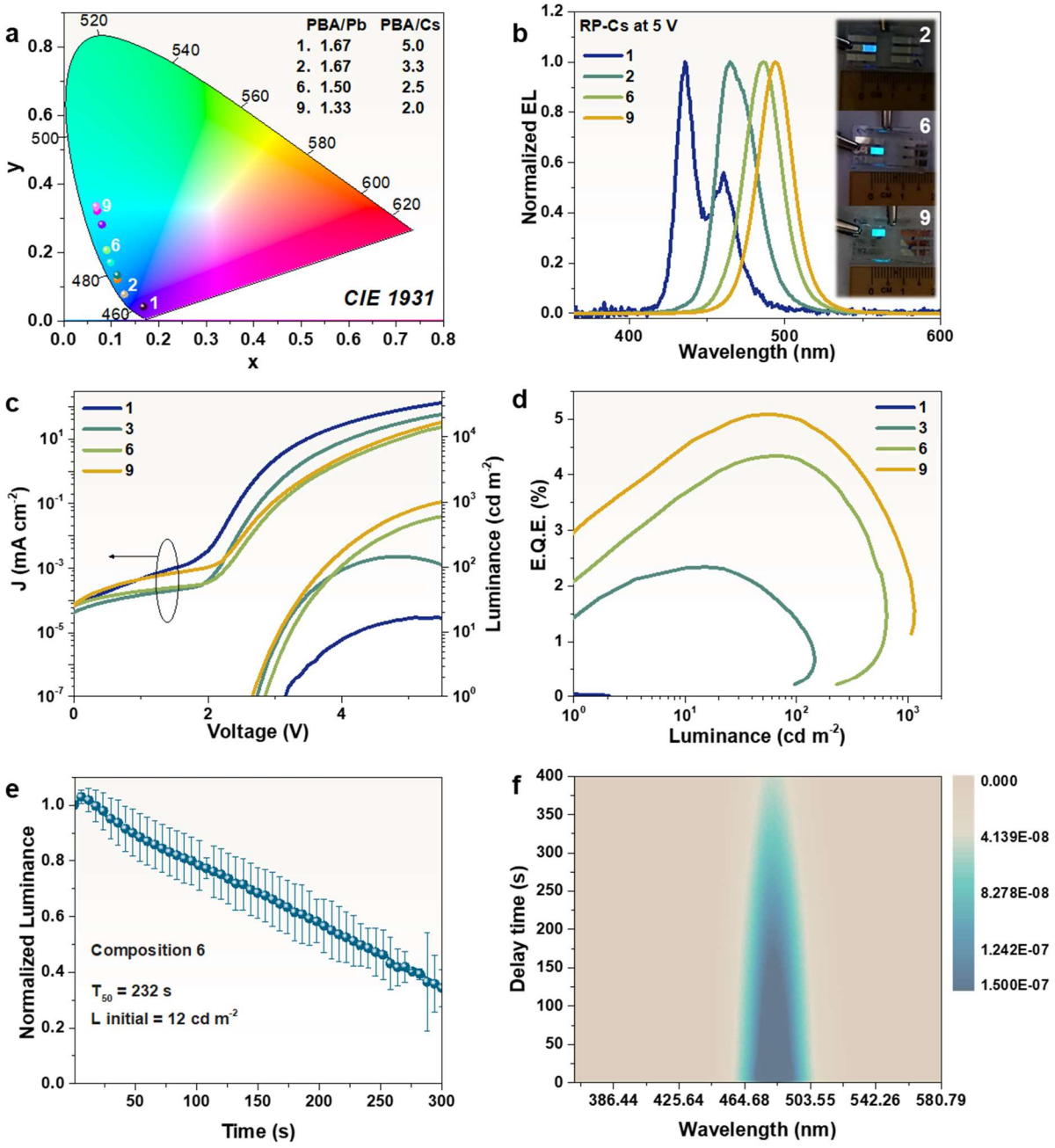

Figure 3. Spectrally tunable blue RP-Cs based light emitting diodes. The CIE coordinates of devices fabricated with various PBA/Pb and PBA/Cs ratios indicating the ease of tailoring the emission across the blue region (a). Normalized EL spectra with images of electrically driven devices fabricated from composition 2, 6 and 9 shown in inset (b), J and luminance curves as a function of voltage (c), and EQE versus luminance (d) of composition no. 1, 2, 6, and 9 indicating that various high efficiency PeLEDs with emissions spanning the blue region can be obtained from a single halide system. The time evolution of luminance (e) and EL spectral profile with increasing delay time (f) for composition no. 6, underlining the spectral stability of the emitter.

Indeed, by tuning both the PBA/Pb and PBA/Cs ratios, LEDs with EL emission ranging from ~437 to ~495 nm can be fabricated (**Figure 3a**). High V_{th}, low efficiency, and a blue shift of EL with increasing bias application are obtained for devices with PBA/Cs ratio of 5 due to the high donor to acceptor ratio (**Figure S7-8**). On lowering PBA/Cs ratio to 3.3 and below, the higher acceptor domain concentration results in the realization of spectrally stable EL despite high bias application (**Figure S8**). Higher EQEs are achieved with lower PBA/Cs ratio regardless of PBA/Pb ratio (**Figure S7**). Overall, maximum EQEs of 2.34, 4.34, and 5.08% are achieved with EL peak at 465, 486, and 493 nm respectively (**Figure 3b-d**, **Figure S9** and **Table S2**). To date, this is the highest reported EQE for bi-cationic, pure bromide-based emissive blue RP perovskite LEDs (**Table S1**) with high efficiency and spectral stability maintained across the blue region. Spectral stability of device 6 is sustained throughout the lifetime measurement set at initial luminance of 12 and 100 $cd.m^{-2}$ (**Figure 3e-f and Figure S10**). Although operational stability is still low, the stable PL spectra and intensity measured for up to 30 min suggest that efficiency and stability of the device are limited by interfacial issues rather than material instability (**Figure S11**).

In summary, relying on a triptych of L and A cation concentrations, solubility limits of A cation, and nucleation kinetics, this report provides a methodology to tailor the perovskite structural landscape to deliver a narrow distribution (m=2-5) of perovskite domains. This controlled distribution of RP domains is essential to ensure efficient blue emission. High concentrations of L cation is necessary to eliminate $m \approx \infty$ domains, whereas the role of the low solubility A-site cation is to curb formation of undesired m= 1 domains. This structural landscape control has enabled record efficiencies of 2.34 and 5.08% corresponding to colour stable deep blue and cyan, respectively for bi-cationic, pure bromide-based emissive blue RP perovskite LEDs. The

single halide system utilized eliminates issues pertaining to halide segregation. This strategy is readily applicable to other L cation systems, leading to significant advancements in blue emission and offers new avenues for CIE colour spectrum tunability.

EXPERIMENTAL METHODS

Procedure for preparation of the 4-phenylbutylammonium bromide salt *(PBABr, $C_6H_5(CH_2)_4NH_3Br$).* To a round bottom flask containing ethanol and 4-phenylbutylamine (PBA), cooled to 0°C, was added a stoichiometric amount of concentrated hydrobromic acid. After stirring the solution (30 min) under the flow of argon, all volatiles were removed using a rotary evaporator. The fine powders, thereby, obtained were washed with copious amounts of diethyl ether, dried under vacuum (50°C) overnight, and transferred into the glovebox. Isolated as a white solid (1.42 g; 92% yield). ^{1}H NMR (400 MHz, DMSO-d6): δ 7.82 (bs, 3 H, NH_3), 7.30-7.15 (m, 5 H, ArH), 2.81-2.78 (m, 2 H, CH_2), 2.60-2.57 (m, 2 H, CH_2), 1.65-1.51 (m, 4 H, CH_2). $^{13}C\{^1H\}$ NMR (100 MHz, DMSO-d6): δ 141.6, 128.3, 128.2, 125.8, 38.6, 34.5, 27.6, 26.5. ^{1}H and $^{13}C\{^1H\}$ NMR spectra of organic compounds were recorded in DMSO-d6 solution using a Bruker Avance 400 spectrometer. Chemical shift values (ppm) are referenced against residual protic solvent peaks.

Perovskite film formation. Depending on the choice of A-cation, mixture of $PbBr_2$, ABr (A: $CH(NH_2)_2^+$, $CH_3NH_3^+$, Cs^+), and $C_6H_5(CH_2)_4NH_3Br$ in DMF: DMSO (64:36) solvent were used to produce the corresponding RP perovskite. To make <m> = 2 solutions with excess $C_6H_5(CH_2)_4NH_3Br$, $PbBr_2$ (0.11 M) is mixed with ABr (0.05 M) and $C_6H_5(CH_2)_4NH_3Br$ (0.165 M) in which the PBA/Pb ratio and PBA/Cs ratio are set to 1.5 and 3.3 respectively. While keeping the $PbBr_2$ concentration fixed (0.11 M), the ratio of ABr and $C_6H_5(CH_2)_4NH_3Br$ are adjusted

accordingly. Films were spin coated from various perovskite solutions at 5000 rpm for 30 s and dried in room temperature. If needed, antisolvent (i.e. toluene) is added 5 s from the initiation of each spin coating process to induce fast nucleation. Both solution preparation and spin coating were done under inert argon environment.

Device fabrication. Poly(3,4-ethylenedioxythiophene)polystyrene sulfonate (PEDOT:PSS, Al 4083) film was fabricated by spin coating at 4000 rpm for 60 s on top of Indium tin oxide (ITO) coated glass. Substrates were then heated (200°C, 40 s) to dry and transported inside the glovebox for perovskite deposition. The electron transporting material ((1,3,5-triazine-2,4,6-triyl)tris(benzene-3,1- diyl))tris(diphenylphosphine oxide) (PO-T2T) (45 nm) and electrode (i.e. LiF (0.8 nm) and aluminum (100 nm)) were deposited via thermal evaporation method. Shadow masks are used during electrode evaporation to define a device area (8mm^2).

Physical characterization. The X-Ray Diffraction (XRD) pattern of the films were recorded using Bruker D8 advance diffractometer with 0D LynxEYE^{TM} detector. Topographical and cross sectional images were captured by employing field effect scanning electron microscope (FE-SEM, JEOL J7600F). Surface roughness measurement was conducted using Atomic Force Microscope (AFM, Asylum Research MFP-3D) under contact modes with Ti/Ir coated cantilevers (ASYELEC-01-R2, Asylum Research). Absorption and steady state PL spectra were collected using Shimadzu UV-3600 UV-Vis-NIR spectrophotometer and Horiba Fluoromax-4 respectively. The transient absorption (TA) measurements were performed using a Helios spectrometer (Ultrafast Systems, LLC). The pump pulse was generated from by a 1 KHz regenerative amplifier [Coherent Legend (150 fs, 1 KHz, 800 nm)] and doubled via second harmonic generation (SHG) by a BBO crystal to obtain 400 nm laser pulses. The regenerative amplifier was seeded by a mode-locked Ti-sapphire oscillator (Coherent Vitesse, 80 MHz). The white light continuum probe beam

(in the range from 410 to 750 nm) was generated by focusing a small portion (~10 μJ) of the fundamental 800 nm laser pulses into a 2 mm sapphire crystal, before filtering out the residual by using 750 nm short-pass filter. Both pump and probe beam were focused onto the sample with $1/e^2$ spot diameter of ~510 μm and ~200 μm, respectively. Meanwhile, the funneling time is estimated from the rise time of the bleaching signal ($\Delta R/R > 0$) of the bulk ($m > 3$) phases at 480 nm. Due to its ultrafast nature, this measured rise signal is the convolution between the exciton funneling time with our system response time (i.e., laser pulse width) of ~190 fs.

Time resolved PL spectra were collected using a Picoquant PicoHarp 300 time correlated single photon counting (TCSPC) system integrated in a micro PL setup. The excitation source was a picosecond pulsed laser diode (Picoquant P-C-405B, λ=405 nm, 40 MHz repetition rate). The luminescence signal was processed through an Acton SP-2300i monochromator coupled to an avalanche diode synchronized with the excitation laser via TCSPC electronics. The overall full width at half maximum of the instrument response function is around 50 ps.

Device characterization. The current-voltage responses of the devices were recorded using Keithley 2612B. Integrating sphere (OceanOptics FOIS-1) coupled with a calibrated spectrometer (OceanOptics QEPro) was used to collect the light emission output. To collect forward light emission only, devices were placed such that the ITO glass is positioned at the opening of the integrating sphere. Absolute irradiance calibration was done by employing Ocean optics HL-3 Plus vis-NIR light source, which was calibrated using a process and documentation based on ISO 17025, IEC Guide 115 and JCGM100:2008 (GUM) protocols

ASSOCIATED CONTENT

Supporting Information.

The following files are available free of charge.

The atomic force microscopy (AFM) images together with topographical and cross-sectional images of RP perovskite films deposited with various A-site cation.

The absorbance and normalized PL intensity spectra of RP films deposited using Cs^+ and phenyl ethyl ammonium (PEA^+) as A-site cation and L cation respectively.

The absorbance spectra evolution versus time of the antisolvent (i.e. toluene) upon addition of RP perovskite precursors with various cations.

The box plot of LED efficiency made with RP-FA, RP-MA, and RP-Cs as the emitter layer.

The electroluminescence (EL) spectra at various bias application for Cs-PBA devices fabricated without the antisolvent technique at <m> = 2.

The absorbance (left) and normalized photoluminescence (right) spectra of films deposited with various PBA/Pb and PBA/Cs ratio.The absorbance (left) and normalized photoluminescence (right) spectra of films deposited with various PBA/Pb and PBA/Cs ratio.

Current density (J) – Voltage (V) – Luminance (L) curves of devices together with the evolution of external quantum efficiency (EQE) versus L for devices fabricated with various PBA/Pb and PBA/Cs ratio.

Normalized electroluminescence (EL) spectra at various bias application for devices fabricated with various PBA/Pb and PBA/Cs ratio.

The box plot of LED efficiency made with RP-Cs composition 1, 2, 6, and 9 as the emitter.

Device operating lifetimes of Device 6 carried out at an initial luminance of ~100 cd m^{-2}.

PL spectra of films before and after constant illuminations.

Summary of work done on PeLEDs emitting at blue region as compared to our data.

Table summary of performance parameters for compositions 1, 2, 6 and 9 consisting of different PBA/Pb and PBA/Cs ratios.

X-Ray Diffraction (XRD) patterns of PBA_2PbBr_4 with d spacing of ~ 2 nm and RP films at <m> = 2 value with various choice of A-site cations indicating similar d spacing (~ 2.74 nm).

Absorbance and normalized photoluminescence spectra for films prepared from (a) RP-FA, (b) RP-MA and (c) RP-Cs solutions, where F, M and C refer to reference films prepared without the use of antisolvents while subscripts T, CF and CB refer to the antisolvent, namely toluene, chloroform and chlorobenzene, respectively.

Ultrafast optical spectroscopy of RP films. Transient absorption (TA) spectra of RP film prepared from <m> = 2 precursor solution with Cs^+ as the A-site cation prepared (a) with and (b) without antisolvent (toluene).

Ultrafast optical spectroscopy of RP films. Transient absorption (TA) spectra of RP film prepared from <m> = 2 precursor solution deposited using antisolvent method with Cs^+ (a) as the A-site cation highlights the propensity for formation of intermediate m domains with low solubility Cs^+ cation. RP-Cs system's spectrally resolved TA kinetics (b) as well as PL kinetics decay (c) and rise times (d) provide evidence of energy funneling in the system and the need to eliminate high m domains ($m \approx \infty$) to obtain pure blue emission.

PL, PL excitation and absorbance spectra of RP-Cs film

Ultrafast optical spectroscopy of RP films. Transient absorption (TA) spectra of RP film prepared from <m> = 2 precursor solution with FA^+ and MA^+ as the A-site cations using antisolvent methods, highlighting the propensity for formation of low m domains with higher solubility FA^+ and MA^+ cations.

AUTHOR INFORMATION

Notes

The authors declare no competing financial interest.

ACKNOWLEDGMENT

This research was funded by National Research Foundation, Prime Minister's Office, Singapore under its Competitive Research Programme (CRP Award No. NRF-CRP14-2014-03), the Intra-CREATE Collaborative Grant (NRF2018-ITC001-001), and Office of Naval Research Global (ONRG-NICOP-N62909-17-1-2155). T.C. S. and D.G. acknowledge the support from the Ministry of Education AcRF Tier 2 grant MOE2017-T2-1-001 and the NRF Investigatorship NRF-NRFI-2018-04. Dr. Sebastian Yongsen Quek is acknowledged for his contribution in absorbance versus time measurement.

REFERENCES

(1) Xing, G.; Mathews, N.; Sun, S.; Lim, S. S.; Lam, Y. M.; Grätzel, M.; Mhaisalkar, S.; Sum, T. C. Long-Range Balanced Electron- and Hole-Transport Lengths in Organic-Inorganic CH3NH3PbI3. *Science.* **2013**, *342* (6156), 344–347. https://doi.org/10.1126/science.1243167.

(2) Edri, E.; Kirmayer, S.; Mukhopadhyay, S.; Gartsman, K.; Hodes, G.; Cahen, D. Elucidating the Charge Carrier Separation and Working Mechanism of CH3NH3PbI(3-x)Cl(x) Perovskite Solar Cells. *Nat. Commun.* **2014**, *5*, 3461. https://doi.org/10.1038/ncomms4461.

(3) Stranks, S. D.; Eperon, G. E.; Grancini, G.; Menelaou, C.; Alcocer, M. J. P.; Leijtens, T.; Herz, L. M.; Petrozza, A.; Snaith, H. J. Electron-Hole Diffusion Lengths Exceeding 1 Micrometer in an Organometal Trihalide Perovskite Absorber. *Science.* **2013**, *342* (6156), 341–344. https://doi.org/10.1126/science.1243982.

(4) Xing, G.; Mathews, N.; Lim, S. S.; Yantara, N.; Liu, X.; Sabba, D.; Grätzel, M.; Mhaisalkar, S.; Sum, T. C. Low-Temperature Solution-Processed Wavelength-Tunable Perovskites for Lasing. *Nat. Mater.* **2014**, *13* (5), 476–480. https://doi.org/10.1038/NMAT3911.

(5) Noh, J. H.; Im, S. H.; Heo, J. H.; Mandal, T. N.; Seok, S. Il. Chemical Management for Colorful, Efficient, and Stable Inorganic − Organic Hybrid Nanostructured Solar Cells. *Nano Lett.* **2013**, *13*, 1764–1769. https://doi.org/dx.doi.org/10.1021/nl400349b.

(6) Deschler, F.; Price, M.; Pathak, S.; Klintberg, L. E.; Jarausch, D. D.; Higler, R.; Hu, S.; Leijtens, T.; Stranks, S. D.; Snaith, H. J.; et al. High Photoluminescence Efficiency and Optically Pumped Lasing in Solution-Processed Mixed Halide Perovskite Semiconductors. *J. Phys. Chem. Lett.* **2014**, *5* (8), 1421. https://doi.org/10.1021/jz5005285.

(7) Tan, Z.-K.; Moghaddam, R. S.; Lai, M. L.; Docampo, P.; Higler, R.; Deschler, F.; Price, M.; Sadhanala, A.; Pazos, L. M.; Credgington, D.; et al. Bright Light-Emitting Diodes Based on Organometal Halide Perovskite. *Nat. Nanotechnol.* **2014**, *9*, 687–692. https://doi.org/10.1038/nnano.2014.149.

(8) Chiba, T.; Hayashi, Y.; Ebe, H.; Hoshi, K.; Sato, J.; Sato, S.; Pu, Y. J.; Ohisa, S.; Kido, J. Anion-Exchange Red Perovskite Quantum Dots with Ammonium Iodine Salts for Highly Efficient Light-Emitting Devices. *Nat. Photonics* **2018**, *12* (11), 681–687. https://doi.org/10.1038/s41566-018-0260-y.

(9) Lin, K.; Xing, J.; Quan, L. N.; de Arquer, F. P. G.; Gong, X.; Lu, J.; Xie, L.; Zhao, W.; Zhang, D.; Yan, C.; et al. Perovskite Light-Emitting Diodes with External Quantum Efficiency Exceeding 20 per Cent. *Nature* **2018**, *562* (7726), 245–248. https://doi.org/10.1038/s41586-018-0575-3.

(10) Kim, J.; Chung, C. H.; Hong, K. H. Understanding of the Formation of Shallow Level Defects from the Intrinsic Defects of Lead Tri-Halide Perovskites. *Phys. Chem. Chem. Phys.* **2016**, *18* (39), 27143–27147. https://doi.org/10.1039/c6cp02886a.

(11) Kumawat, N. K.; Liu, X. K.; Kabra, D.; Gao, F. Blue Perovskite Light-Emitting Diodes: Progress, Challenges and Future Directions. *Nanoscale* **2019**, *11* (5), 2109–2120. https://doi.org/10.1039/c8nr09885a.

(12) Manser, J. S.; Christians, J. A.; Kamat, P. V. Intriguing Optoelectronic Properties of Metal Halide Perovskites. *Chem. Rev.* **2016**, *116* (21), 12956–13008. https://doi.org/10.1021/acs.chemrev.6b00136.

(13) Saparov, B.; Mitzi, D. B. Organic-Inorganic Perovskites: Structural Versatility for Functional Materials Design. *Chem. Rev.* **2016**, *116* (7), 4558–4596. https://doi.org/10.1021/acs.chemrev.5b00715.

(14) Cao, D. H.; Stoumpos, C. C.; Farha, O. K.; Hupp, J. T.; Kanatzidis, M. G. 2D Homologous Perovskites as Light-Absorbing Materials for Solar Cell Applications. *J. Am. Chem. Soc.* **2015**, *137* (24), 7843–7850. https://doi.org/10.1021/jacs.5b03796.

(15) Xing, J.; Zhao, Y.; Askerka, M.; Quan, L. N.; Gong, X.; Zhao, W.; Zhao, J.; Tan, H.; Long, G.; Gao, L.; et al. Color-Stable Highly Luminescent Sky-Blue Perovskite Light-Emitting Diodes. *Nat. Commun.* **2018**, *9* (1), 1–8. https://doi.org/10.1038/s41467-018-05909-8.

(16) Quan, L. N.; Zhao, Y.; García De Arquer, F. P.; Sabatini, R.; Walters, G.; Voznyy, O.; Comin, R.; Li, Y.; Fan, J. Z.; Tan, H.; et al. Tailoring the Energy Landscape in Quasi-2D Halide Perovskites Enables Efficient Green-Light Emission. *Nano Lett.* **2017**, *17* (6), 3701–3709. https://doi.org/10.1021/acs.nanolett.7b00976.

(17) Yuan, M.; Quan, L. N.; Comin, R.; Walters, G.; Sabatini, R.; Voznyy, O.; Hoogland, S.; Zhao, Y.; Beauregard, E. M.; Kanjanaboos, P.; et al. Perovskite Energy Funnels for Efficient Light-Emitting Diodes. *Nat. Nanotechnol.* **2016**, *11* (10), 872–877. https://doi.org/10.1038/nnano.2016.110.

(18) Jiang, Y.; Qin, C.; Cui, M.; He, T.; Liu, K.; Huang, Y.; Luo, M.; Zhang, L.; Xu, H.; Li, S.; et al. Spectra Stable Blue Perovskite Light-Emitting Diodes. *Nat. Commun.* **2019**, *10* (1), 1868. https://doi.org/10.1038/s41467-019-09794-7.

(19) Liu, Y.; Cui, J.; Du, K.; Tian, H.; He, Z.; Zhou, Q.; Yang, Z.; Deng, Y.; Chen, D.; Zuo, X.; et al. Efficient Blue Light-Emitting Diodes Based on Quantum-Confined Bromide Perovskite Nanostructures. *Nat. Photonics* **2019**. https://doi.org/10.1038/s41566-019-0505-4.

(20) Oswald, I. W. H.; Koegel, A. A.; Neilson, J. R. General Synthesis Principles for Ruddlesden–Popper Hybrid Perovskite Halides from a Dynamic Equilibrium. *Chem. Mater.* **2018**, *30*, 8606–8614. https://doi.org/10.1021/acs.chemmater.8b03817.

(21) Hu, Y.; Spies, L. M.; Alonso-Álvarez, D.; Mocherla, P.; Jones, H.; Hanisch, J.; Bein, T.;

Barnes, P. R. F.; Docampo, P. Identifying and Controlling Phase Purity in 2D Hybrid Perovskite Thin Films. *J. Mater. Chem. A* **2018**, *6* (44), 22215–22225. https://doi.org/10.1039/C8TA05475D.

(22) Quintero-Bermudez, R.; Gold-Parker, A.; Proppe, A. H.; Munir, R.; Yang, Z.; Kelley, S. O.; Amassian, A.; Toney, M. F.; Sargent, E. H. Compositional and Orientational Control in Metal Halide Perovskites of Reduced Dimensionality. *Nat. Mater.* **2018**, *17* (10), 900–907. https://doi.org/10.1038/s41563-018-0154-x.

(23) Zhou, N.; Shen, Y.; Li, L.; Tan, S.; Liu, N.; Zheng, G.; Chen, Q.; Zhou, H. Exploration of Crystallization Kinetics in Quasi Two-Dimensional Perovskite and High Performance Solar Cells. *J. Am. Chem. Soc.* **2018**, *140* (1), 459–465. https://doi.org/10.1021/jacs.7b11157.

(24) Liang, K.; Mitzi, D. B.; Prikas, M. T. Synthesis and Characterization of Perovskite Films Using Two-Step Dipping Technique. *Chem. Mater.* **1998**, *10* (1), 403–411. https://doi.org/10.1021/cm970568f.

(25) Chiang, C. H.; Wu, C. G. A Method for the Preparation of Highly Oriented MAPbI3 Crystallites for High-Efficiency Perovskite Solar Cells to Achieve an 86% Fill Factor. *ACS Nano* **2018**, *12*, 10355–10364. https://doi.org/10.1021/acsnano.8b05731.

(26) Svane, K. L.; Forse, A. C.; Grey, C. P.; Kieslich, G.; Cheetham, A. K.; Walsh, A.; Butler, K. T. How Strong Is the Hydrogen Bond in Hybrid Perovskites? *J. Phys. Chem. Lett.* **2017**, *8* (24), 6154–6159. https://doi.org/10.1021/acs.jpclett.7b03106.

(27) Yantara, N.; Bruno, A.; Iqbal, A.; Jamaludin, N. F.; Soci, C.; Mhaisalkar, S.; Mathews, N. Designing Efficient Energy Funneling Kinetics in Ruddlesden–Popper Perovskites for High-Performance Light-Emitting Diodes. *Adv. Mater.* **2018**, *30* (33). https://doi.org/10.1002/adma.201800818.